Journal of Sound and Vibration 540 (2022) 117305

Contents lists available at ScienceDirect

Journal of Sound and Vibration

journal homepage: www.elsevier.com/locate/jsvi

Physical realization and experimental validation of effective phononic crystals for control of radial torsional waves

Ignacio Arretche *, Kathryn H. Matlack

Department of Mechanical Science and Engineering, University of Illinois Urbana-Champaign, 1206 W Green St., Urbana, IL, 61801

ARTICLE INFO

Keywords:
band gaps
torsional vibrations
metamaterials
phononic crystals
radial waves
experimental validation

ABSTRACT

Recently, the concept of effective phononic crystals (EPCs) and locally resonant effective phononic crystals (LREPCs) have been proposed to enable properties of phononic crystals (PCs) and acoustic metamaterials (AMs), respectively, in radially propagating waves. This problem is not straightforward since the equations of motion of radially periodic systems do not have periodic coefficients and thus Bloch solutions in these radially periodic systems are not valid. To overcome this, EPCs and LREPCs use radially dependent properties to force periodic coefficients in the equations of motion of radial elastic waves, enabling the application of the Bloch theorem and thus allowing for properties of PCs and AMs. However, the required radially dependent properties severely complicate their physical realization, since modulus and density must be tailored such that they follow a specific radial variation. In this paper, we propose a method to physically realize an LREPC by radially varying its impedance through spatial changes to its out-of-plane thickness. Physical realization of the LREPC also involves local torsional resonances. In contrast to typical AMs, the resonators in the LREPC must be geometrically different to retain the same torsional stiffness and moment of inertia at different radii. We use additive manufacturing plus traditional machining to fabricate the LREPC. We introduce an experimental setup to measure radially propagating torsional waves in the LRPEC and show how to decouple torsional vibrations from bending vibrations to accurately measure transmission. To show the importance of using an LREPC, we compare its dynamic response to a locally resonant homogenous system (LRHS), a system that is radially periodic but has non-periodic equations of motion. Measured transmission shows that only the LREPC attenuates waves inside the band gap frequencies predicted by Bloch analysis. This work experimentally shows that LREPCs allow for the application of well-known concepts of AMs to control radially propagating torsional waves.

1. Introduction

Phononic crystals (PCs) and acoustic metamaterials (AMs) have shown great promise when it comes to wave propagation control [1]. Through PCs and AMs phenomena like band gaps [2,3], negative refraction [4], negative effective properties [5], and topological states [6] are possible. Because of the inherent periodicity of PCs and the typically periodic AM designs, using the Bloch theorem to calculate the band structure has become the essential way to analyze and design PCs and AMs. PCs require geometrical periodicity, which can be achieved through differences in cross-sectional areas [7], lattice structures [8,9], and multiple materials [10–12]. AMs,

* Corresponding author:
E-mail address: ia6@illinois.edu (I. Arretche).

https://doi.org/10.1016/j.jsv.2022.117305
Received 28 April 2022; Received in revised form 8 August 2022; Accepted 12 September 2022
Available online 13 September 2022

on the other hand, require resonances, which can be physically realized using either soft material layers [5,13] or compliant elements [4,14–16] that connect a large mass in parallel to an underlying matrix. Experimental validation of PCs and AMs has also been widely done using different types of excitation and acquisition techniques for longitudinal waves [10,17,18], shear waves[19], and bending waves [7,11]. However, most studies assume plane waves in their analysis and validation. The plane wave assumption is not always valid. For example, in waves that propagate radially from a small radius, wavefronts take a cylindrical form (i.e. radial waves and not plane waves).

The control of radial waves using PCs and AMs significantly complicates the analysis, physical realization, and experimental validation. From an analysis standpoint, the equations of motion that describe radial waves in a geometrically periodic system (i.e. a system formed by spatial tessellation of a unit cell in the radial direction) do not have periodic coefficients. Thus, the Bloch theorem cannot be applied, and so canonical properties of geometrically periodic PCs and AMs do not necessarily exist for radial waves. When analyzing PCs and AMs for radial waves, there are two main approaches. One approach is to use a geometrically periodic system and either analyze finite structures [20–22], use a modified Wave Finite Element approach [23], or assume large radii [24,25]. The limitation of this approach is that there is no certainty that known properties of PCs and AMs that arise from Bloch analysis will hold, particularly at the smaller radii, and one must specifically design the finite system. An alternative approach is to look for a certain set of material properties that, despite breaking geometrical periodicity, enforce the periodic coefficients in the equations of radial waves. In this area, radial wave crystals (RWCs) have been proposed, which have radially varying anisotropic density/ permeability such that the acoustic/ electromagnetic wave equations in radial coordinates have periodic coefficients [26]. Our recent work [27] shows that this also is possible for elastic waves using effective phononic crystals (EPCs), which force periodic coefficients using radially varying isotropic material properties. Their name comes from the fact that although these systems break geometric periodicity, their behavior is effectively described by a periodic partial differential equation. EPCs support band gaps and topologically protected states in radial waves because their equations of motion are equivalent to those of the well-known Cartesian PCs (i.e. PCs described by lattice vectors in a Cartesian coordinate system). EPCs and RWCs are based on Bragg scattering mechanisms, however, our recent study has extended the concept of EPCs to include local resonances by introducing locally resonant effective phononic crystals (LREPCs) [28]. Using LREPCs, properties of Cartesians AMs, such as locally resonant band gaps and negative effective properties, can be extended to radial waves.

Even though RWCs, EPCs, and LREPCs have been shown numerically to control radial waves, they require a specific radial dependence of material properties, making them challenging to physically realize. In fact, only a simplified version of RWCs has been physically realized for electromagnetic waves [29] using a series of split ring resonators. However, these RWCs are simplified such that only one of its three constitutive parameters follows the necessary radial dependence, and this constitutive parameter is approximated by a stepped function (which only works if wavelengths are large enough). Further, because it consists of split-ring resonators, it can achieve tailored properties only around a design frequency, making it somewhat narrow banded. The acoustic counterparts of RWCs require anisotropic density, which could be realized through periodic cylindrical multilayers [30], however, several layers are needed to obtain a single value of anisotropic density, resulting in a complicated design. This is possibly the reason why RWCs have not been physically realized in the acoustic domain. On the other hand, EPCs and LRPECs do not require anisotropic density and can be realized using isotropic materials properties. This makes them potentially simpler to realize. However, they also involve the challenge of a specific radial dependence of impedance and thus, also remain to date a purely analytical/ numerical construction.

Although the concept of EPC and LREPC is independent of wave polarization and can be applied, for example, to longitudinal radial waves [27], we will focus in this paper on addressing radial torsional waves. In fact, although torsional waves can be detrimental to rotating machinery such as turbines, compressors, or engines [31], the application of PCs and AMs to torsional waves is actually quite limited. There are a few studies [32,33] that, under plane wave assumptions (i.e. axial torsional waves), propose adding torsional resonators to a cylindrical axis to impose band gaps, but these remain purely numerical. Even under the plane wave assumption, experimental studies of PCs and AMs for torsional waves are scarce. This is because excitation (e.g. electrodynamic shakers, transducers) and measurement (e.g. accelerometers, laser vibrometers) equipment typically aim to excite/measure translational displacements or velocities. Thus, extra elements in the setup are needed to ensure an accurate excitation and measurement of torsional waves. In this area, Ma et. al. [13] proposed using a DC motor as an excitation source and Cabaret et. al. [34] used an electrodynamic shaker to excite torsional waves. However, both these studies are for plane waves. Studies of PCs and AMs related to controlling radial torsional waves remain purely analytical or numerical [20,27,28]. Experimental measurement of the transmission of radial torsional waves is more challenging compared to plane waves. In these measurements, bending waves may dominate the results at low frequencies because the mass of the sample is axially distributed in a small region of the excitation axle, lowering the bending natural frequencies of the setup and preventing pure torsional excitation while testing. Thus, data postprocessing must be done to decouple possible torsional and bending modes of vibrations, especially inside torsional band gaps where displacement amplitudes of torsional waves can be in the same order as those of bending waves.

In this paper, we physically realize and experimentally validate the concept of effective periodicity. We concentrate on the physical realization of an LREPC because its physical realization involves not only achieving radially varying properties but also designing torsional resonators. In addition, band gaps in LREPCs show larger differences with respect to their non-effectively periodic counterpart compared to the EPC[28]. However, the approach presented here can also be used to physically realize and experimentally validate EPCs. First, we briefly derive the concept of effective periodicity, which was thoroughly derived previously[27,28], using a 1D model that assumes axisymmetric wave propagation, plane displacements, and lumped mass-spring resonators. We also introduce a system that has geometric periodicity but no effective periodicity, which we call the locally resonant homogenous system (LRHS). Throughout the paper, we compare the LRHS to LREPC to show the importance of effective periodicity in radial waves. We propose to physically realize the LREPC by radially varying the thickness. The variation in thickness causes a radial variation in the impedance,

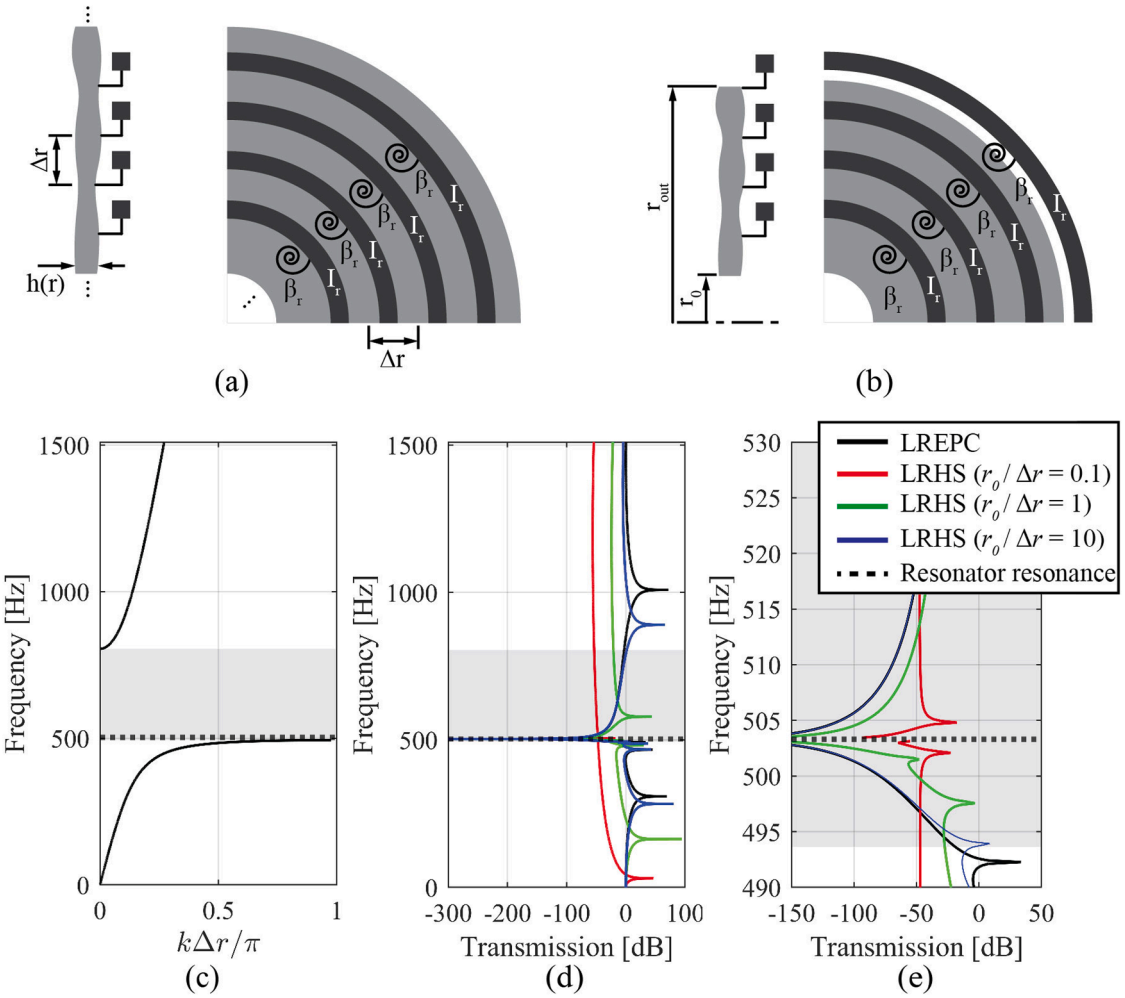

Fig. 1. (a) Infinite and (b) 4-unit cell finite LRPEC with varying out-of-plane thickness. (c) band structure of an LREPC. (d) Transmission curves of an LREPC and an LRHS for different values of $r_0/\Delta r$. (e) Zoom in view of transmission in the neighborhood of the resonance frequency of the resonators.

imposing effective periodicity on the system while easing physical realization. To bring the resonator from a lumped mass-spring model to a physical model, we use soft, light rings (as torsional springs) attached to stiff, heavy rings (as mass moment of inertias). In contrast to local resonances in Cartesian AMs, we shall see that to keep stiffness and inertias the same in all unit cells, the resonators must be geometrically different. Thus, there is an effective periodicity that arises from the realization of the local resonances, in addition to the effective periodicity of the underlying matrix. 3D finite element modeling results explain slight differences in the behavior of the proposed physical realization and the 1D axisymmetric model. We then combine voxel-based additive manufacturing and machining to fabricate the proposed LREPC and LRHS and characterize the viscoelastic properties of the constituent materials using beam-like specimens [35]. We present an experimental setup capable of accurately measuring the transmission of radial torsional waves to experimentally validate our results. The setup uses an electrodynamic shaker and a single-point laser vibrometer typically used to validate Cartesian PCs and AMs. We decouple torsional and bending vibrations by data postprocessing of multiple input and output measurements, without the need for a special dual-beam laser[36]. We compare the experimental transmission of the LREPC with analytical band gap ranges and with the experimental transmission of the LRHS to show that the LREPC effectively behaves as a periodic system and that it attenuates radial torsional waves over a broader band of frequencies compared to the LRHS.

2. Effective periodicity in radial torsional waves

Assuming axisymmetric wave propagation and displacements that are independent of the out-of-plane direction, the equations of motion that describe a radial torsional wave propagating through a heterogeneous continuum medium with equally spaced lumped mass-spring local resonances and variable out-of-plane thickness are (Fig. 1(a)),

$$\begin{cases} r^3 B(r)\dfrac{\partial^2\theta(r,t)}{\partial t^2} = \dfrac{\partial}{\partial r}\left(r^3 A(r)\dfrac{\partial\theta}{\partial r}\right) + \sum_i \beta_r(\theta(r_i,t)-\theta_i(t))\delta(r-r_i) \\ I_r\dfrac{d^2\theta_i(t)}{dt^2} = \beta_r(\theta_i(t)-\theta(r_i,t)) \end{cases} \tag{1}$$

where $B(r) = 2\pi\rho(r)h(r)$, $A(r) = 2\pi\mu(r)h(r)$, μ and ρ are the shear modulus and the density of the *matrix* (material to which resonators are attached to - light gray in Fig. 1), h is the out-of-plane thickness, δ is the Kronecker-Delta function, β_r and I_r are torsional stiffness and mass moment of inertia of the resonators, respectively, θ_i is the angular displacement of resonator i, $r_i = r_0 + i\Delta r$ is the location of resonator i and r_0 is the internal radius of the system. In Eq. (1), if h, μ, and ρ are independent of radius (i.e. $B(r) = B_{0HS}$ and $A(r) = A_{0HS}$), then the equations of motions lack translational invariance of the form $r \to r + n\Delta r$, where n is an integer. Thus, the Bloch theorem cannot be applied in this case and typical properties of PCs and AMs derived from this theorem may no longer be valid. We call this radially independent system the locally resonant homogenous system (LRHS) because its matrix is made of a homogenous material. Note that this system is geometrically periodic, since the radial tessellation of its unit cell results in the full system, but not effectively periodic since its equations of motion do not have periodic coefficients. We use the LRHS as a benchmark to show the importance of the effective periodicity approach.

The concept of effective periodicity [27,28] consists of identifying a set of material properties that results in radial equations of motion that have periodic coefficients. This allows us to apply the Bloch theorem to radial torsional waves and enable canonical properties of PCs and AMs for radial waves. To achieve effective periodicity, we inspect Eq. (1) and choose a set of properties that result in equations that have periodic coefficients and thus accept a Bloch wave solution. We can do this by setting,

$$\begin{cases} A(r) = \dfrac{A_0}{r^3} \\ B(r) = \dfrac{B_0}{r^3} \end{cases} \tag{2}$$

where A_0 and B_0 are constants. In this way, Eq. (1) can be solved using the Bloch theorem. We can even define a unit cell based on the equation of motion and obtain a close-form solution for the dispersion of the infinite system [28] (Fig. 1(c)). We call this system a locally resonant effective phononic crystal (LREPC). The LREPC supports typical properties of locally resonant systems such as band gaps and negative effective inertia in radial waves. For more detail on effective periodicity, we refer the reader to references [27,28].

A meaningful comparison between LREPC and LRHS can be made by either enforcing equal mass, stiffness, and frequency ratios between the systems or by enforcing equal static torsional stiffness and resonators between the systems (see [28] for more detail). Here, we use the former, since the resonators of LRHS and LREPC are the same, avoiding potential differences in transmission between the LREPC and LRHS that may arise from a lump mass-spring approximation of the physical models. However, the method of physical realization presented herein could be extended to the other comparisons as well.

For LREPC and LRHS to have the same static torsional stiffness, the properties of the LRHS must be,

$$\begin{cases} A_{0HS} = \dfrac{A_0(r_{out}+r_0)}{2r_{out}^2 r_0^2} \\ B_{0HS} = \dfrac{B_0 A_{0HS}}{A_0} \end{cases} \tag{3}$$

where r_{out} is the external radius of the finite system (Fig. 1(b)). Since the LRHS does not support band gaps (because it is not effectively periodic) we compare the systems in terms of transmission of a 4-unit cell finite system (Fig. 1(b)). Throughout this paper, the transmission of torsional waves is defined as the ratio of angular displacement at the outer ring (r_{out}) to angular displacement at the inner ring (r_0). We define transmission in terms of angular displacements because the equation with periodic coefficients is in terms of angular displacements (Eq. (1)) and thus, we expect the LREPC to behave as effectively periodic in terms of angular displacements. We calculate the transmission based on the axisymmetric 1D equation (Eq. (1)) in Matlab using a 1D finite element code.

To briefly illustrate the importance of effective periodicity we calculate the band structure (Fig. 1(c)) and transmission (Fig. 1(d)) of a typical LREPC and compare it with the transmission curves (Fig. 1(d)) of the LRHS that has the same static torsional stiffness and resonators (Eq. (3)). The drop in transmission of the LREPC agrees well with the predicted band gap range. The LREPC dynamic behavior is also independent of r_0, thus, it's independent of where we decide to truncate the system (a property that characterizes periodic systems). Thus, the finite LREPC behaves as a periodic system despite its geometric aperiodic radial structure. In the case of the LRHS, the system shows different behavior from that of a periodic system (Fig. 1(d)). First, the transmission is strongly dependent on r_0 and second, the dynamic behavior is very different from what is expected from the band structure even close to the resonance frequency of the resonators (Fig. 1(e)). Thus, we need effective periodicity (i.e. an LREPC) to apply concepts that arise from band structure to radial waves. As $r_0/\Delta r$ increases, the transmission curves of the LREPC and LRHS approximate each other. At large radii, the wave in the LRHS approximates a plane wave and thus, a radial periodic approximates a Cartesian periodic system.

3. Physical implementation of LREPC design

The main challenge in physically realizing effective periodicity is that the required material properties, i.e. $A(r)$ and $B(r)$, must scale

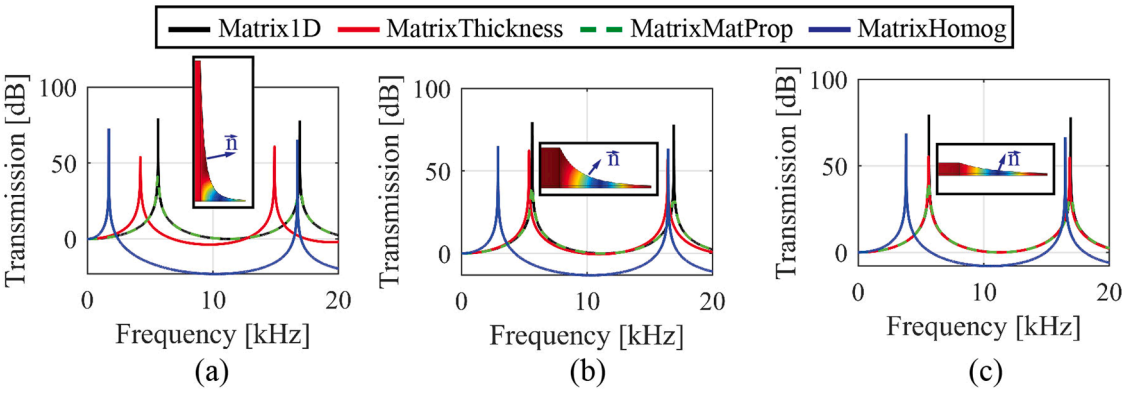

Fig. 2. Transmission curves for matrix material with no resonators. (a) $\frac{r_0}{\Delta r} = 1$, (b) $\frac{r_0}{\Delta r} = 2.5$, and (c) $\frac{r_0}{\Delta r} = 5$. Insets show normalized angular displacements for MatrixThickness at 10kHz. The normal to the traction free surface is also shown in these insets.

with $1/r^3$ (Eq. (2)). Further, the LREPC requires local resonances, which will turn out to be all geometrically different to keep their stiffnesses and moment of inertias the same for all unit cells. As expected, there are certain discrepancies in behavior when going from an idealized axisymmetric 1D model (Section 2) to a 3D physical model. To understand these discrepancies for the LREPC, we first study the response of the physical models of the matrix and resonators independently and then of the full 3D physical model of the LREPC.

Eq. (2) shows that the required $A(r)$ and $B(r)$ can be obtained either by varying μ and ρ with radius and keeping h constant or by keeping μ and ρ constant and varying h with radius. While different lattice materials could be used to obtain a variety of material properties (particularly stretch-dominated lattices where density and moduli are proportional [37,38]), the design of lattice materials for such a purpose is challenging since it requires small lattice constants to obtain the needed long-wavelength limit behavior of the matrix at the frequencies of the resonators. In addition, generating lattice geometries in radial coordinates poses extra challenges in terms of how to spatially distribute the unit cells and a cylindrical mapping would be needed[39]. Instead, we propose here a much simpler approach: varying thickness while keeping material properties constant.

The main limitation of taking this approach is that as thickness varies, a free boundary forms with a surface normal component in the radial direction (Fig. 2 - insets). To comply with the free boundary, the angular displacements become thickness dependent, which breaks the assumption of thickness independence of Eq. (1). At the smaller inner radii, the radial component of the normal vector is larger and thus the approach will be limited to some minimum radius. To understand the range of validity of the approach, we run 3D finite element simulations on 4-unit cell matrices (without resonators) using COMSOL Multiphysics for different $r_0/\Delta r$. We calculate transmission of three different systems: one where we vary the thickness and keep material properties constant (MatrixThickness), one where we vary material properties and keep thickness constant (MatrixMatProp), and a third one where we keep material properties and thickness constant (MatrixHomog) – refer to Table A1 (Appendix A). Note that MatrixThickness is what we will use for the physical realization of the LREPC and MatrixHomog is what we will use for the LRHS.

We run a frequency sweep analysis in which we excite the center ring with an angular harmonic displacement and measure transmission as the ratio of average angular displacements at the outermost cylindrical surface, i.e. at a radius $r_{out} = r_0 + 4\Delta r$, to average angular displacement on the center ring. The material properties of MatrixThickness and MatrixHomog are constant and equal to the average over frequency of VeroWhite material, which we will later use for fabrication (Section 4). The out-of-plane thickness of the MatrixThickness is varied according to Eq. (2) and A_0 is selected such that the minimum thickness (i.e. the thickness at the outer ring) is equal to 1mm, which is the minimum feature size we can fabricate. The out-of-plane thickness of the MatrixHomog is constant and such that it complies with Eq. (3). Finally, the MatrixMatProp has a constant thickness of 8mm and its material properties are defined such that A_0 and B_0 are the same as those of MatrixThickness (Eq. (2)). We do not include damping nor frequency dependence of material properties, to isolate effects of thickness variation from those of viscoelasticity. We compare the transmission of these three systems with the transmission of the matrix under the idealized axisymmetric 1D assumption of Section 1 (Eq. (1) with $\beta_r = 0$). We refer to the latter as Matrix1D. The goal is to obtain a response of the matrix of our physical model that is as close as possible to that of the Matrix1D.

Simulations show that transmission of MatrixMatProp and Matrix1D are essentially the same for all $r_0/\Delta r$. This is because the top and bottom free boundaries of MatrixMatProp have a normal with no radial component. Thus, the angular displacements are thickness independent and the 3D physical model of the MatrixMatProp closely follows the assumptions of the 1D model. For the MatrixThickness, the curvature of the free boundary is large at low $r_0/\Delta r$, resulting in significant thickness dependence of angular displacements (Fig. 2(a) – inset) and thus, large differences in behavior compared to the Matrix1D (Fig. 2(a)). As we increase $r_0/\Delta r$, the curvature decreases, the 3D effects decrease and thus the MatrixThickness approximates the Matrix1D (Fig. 2(b-c)). The behavior of the MatrixHomog is quite different for all three $r_0/\Delta r$ values shown in Fig. 2. This shows that the MatrixThickness approximates the behavior of the Matrix1D because of the decrease in 3D effects, not from a possible plane wave approximation at a large radius. For physical realization, we choose $r_0/\Delta r = 2.5$ because it is sufficiently close to the response of the Matrix1D while keeping the effects of

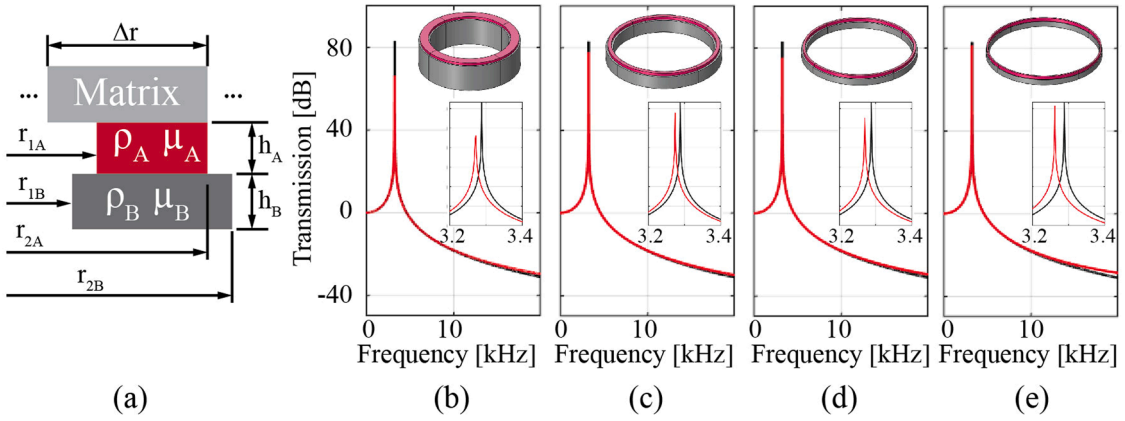

Fig. 3. (a) Schematic of the torsional resonator design. (b-e) 3D finite element calculated response (red) and 1-dof analytical response (black) for resonators of units 1-4, respectively. Top-right insets show resonators and center-right insets zoom-in view in the neighborhood of the resonance peak.

radial waves (Fig. 2(b)).

Now that we have chosen a physical model for the matrix of the LREPC, we must come up with a physical model of the resonators. The physical implementation of idealized local resonances (lumped mass-spring) has been extensively studied for Cartesian locally resonant systems [5,13], however, some essential differences arise for the radially spaced torsional resonators of the LREPC. Generally, lumped mass-spring local resonances are physically realized by a soft/light component that acts as the spring and a stiff/heavy component that acts as the mass. In our case, given that we are looking at torsional resonators (i.e. torsional springs and mass moment of inertias) the resonator is composed of a soft, light ring, *Ring A* that acts as the spring, and a stiff, heavy ring, *Ring B* that acts as the mass moment of inertia (Fig. 3(a)). Ring A is attached to the matrix on one face and to Ring B on the opposite face. The torsional stiffness and inertias of these rings can be calculated as,

$$\beta_i = \frac{\mu_i \pi \left(r_{2i}^4 - r_{1i}^4\right)}{2h_i} \tag{4}$$

$$I_i = \frac{\rho_i h_i \pi \left(r_{2i}^4 - r_{1i}^4\right)}{2} \tag{5}$$

where $i = A, B$ for Ring A and Ring B, respectively Fig. 3(a)). We choose the outer radius of Ring A to be the same as the outer radius of the unit cell (i.e $r_{2a} = r_0 + (N+1)\Delta r$). We then calculate its inner radius and its thickness to obtain the required stiffness. Ring B is placed such that its mid radius coincides with that of Ring A. Its inner radius, outer radius, and thickness are selected to calculate the required moment of inertia. Note that there is no unique way of defining the thickness and radii of each ring as any combination that complies with the required stiffness for Ring A, and inertia for Ring B would be valid (Eq. (4) and ((5)). However, to ensure the system approximates the lumped mass-spring model in Section 1, the stiffness and moment of inertia of Ring B must be large compared to that of Ring A. Thus, we iterate until we obtain a moment of inertia and stiffness of Ring B that is at least 20 times that of Ring A. To characterize the effects of resonator design from those that may arise from viscoelasticity, we first assume no damping and frequency-independent material properties. We use average moduli over frequency of FLX9895 (Section 4), which we will use for fabrication, for Ring A, and material properties of mild steel for Ring B. The resulting resonator geometries are shown in the insets of Fig. 3(b-e).

Clearly, there is an essential difference between these physically implemented torsional resonators and those typical of Cartesian systems: for all resonators to have the same torsional stiffness and mass moment of inertia, they must all be geometrically different. Thus, there is also an effective periodicity (i.e. periodicity of equations of motion but not of geometry) involved in the design of the local resonances. In Cartesian systems, all resonators are geometrically the same and thus, typical differences between the response of a 3D model and its lumped mass-spring model approximation are the same for all resonators [14,16]. However, in the LREPC, the resonators are all geometrically different and thus these differences will be slightly different. In addition, these resonators are only tuned to be the same at their first resonance and not at higher resonances, so the effective periodicity does not exist at higher frequencies.

To characterize the effect of geometrical differences in the resonators, we conduct a 3D finite element simulation in COMSOL Multiphysics of each of the four resonators. We prescribe a harmonic displacement on the upper face of Ring A and measure the angular displacement at the lower face of Ring B. We calculate the response as input to output angular displacement and compare it to the analytical response of a lumped mass-spring system (the ideal resonator) with the corresponding stiffness and moment of inertia (Fig. 3 (b-e)). Generally, the response of the 3D resonators agrees quite well with that of the lumped mass-spring system, which is evidence that the physical model behaves as a local resonance. However, we not only observe slight differences in the resonance peak of the physical model compared to the lumped mass-spring model (something typical when physically realizing a lumped mass-spring model) but also that these differences are slightly different for the different resonators, i.e. resonators are slightly mistuned with respect to

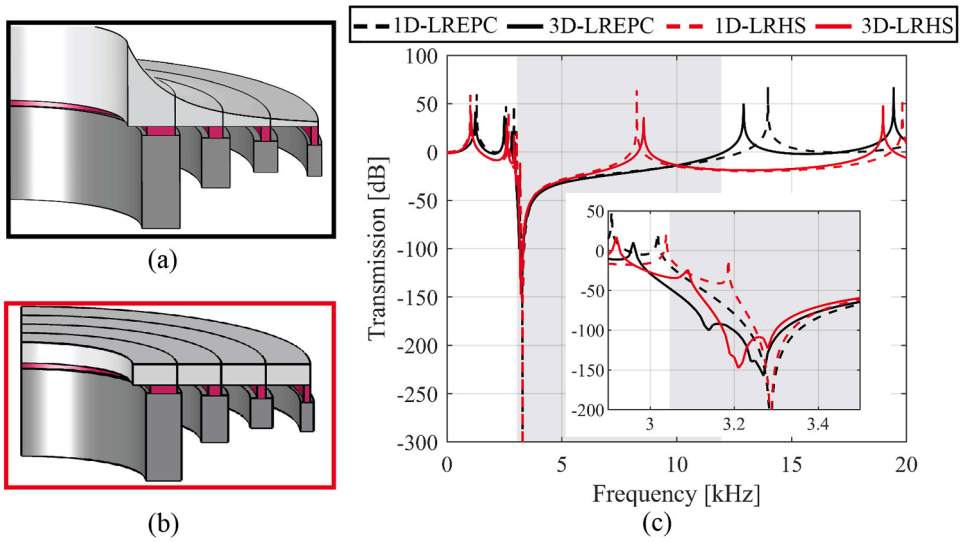

Fig. 4. 3D-LREPC (a) and 3D-HS (b). Only a quarter of the system is shown. (c) Transmission curves for 1D and 3D LREPC and HS. Inset shows zoom in view of transmission in vicinity of the lower band gaps edge. The shaded region is the predicted band gap from LREPC band structure.

each other. In addition, the physical 3D resonators are a continuous system and as such, they have higher-order modes. Therefore, the 3D model deviates from the lumped mass-spring model at higher frequencies. The resonators are tuned such that their first resonance is the same, however, higher resonances will not necessarily be the same (again because they are geometrically different) and thus, this higher frequency region deviates more from the lumped mass-spring response for resonators 3 and 4 (Fig. 3(d-e)) than for resonators 1 and 2 (Fig. 3(b-c)). Overall, the effective periodicity is achieved within a certain frequency range but with a slight mistuning, however, at higher frequencies, all resonators respond differently. These geometrical differences are not present in the Cartesian system and will have some effects on the response of the 3D physical model of the LREPC.

Finally, we combine the matrix material with the resonator design to obtain the full physical model of the LREPC Fig. 4(a)) and the LRHS (Fig. 4(b)). In this section, we refer to these physical models that consider 3D displacements as 3D-LREPC (3D-LRHS) (Fig. 4(a-b)) and the idealized axisymmetric 1D case (Eq. (1) and Fig 1(b)) as 1D-LREPC (1D-LRHS) – refer to Table A1 (Appendix A). We calculate the transmission of 3D-LREPC and 3D-LRHS using finite element simulations and compare it with the 1D-LREPC and 1D-LRHS, respectively (Fig. 4(c)). We also calculate the closed-form dispersion of the LREPC (using Bloch theorem and Eqs. (1) and ((2) [28]), and plot band gap ranges as shaded regions in Fig. 4(c). Note that the 1D-LRHS is geometrically periodic, however, the 3D-LRHS has a constant matrix (which is geometrically periodic by definition) and effectively periodic resonators. However, we expect the behavior of the 1D-LRHS and the 3D-LRHS to be nominally the same.

Overall, there is good agreement between the 3D and the 1D systems for both the LREPC and the LRHS, particularly in the lower frequency range (Fig. 4(c)). The differences in transmission become larger as frequency increases. At higher frequencies, the transmission shifts toward lower frequencies for both 3D-LREPC and 3D-LRHS compared to the 1D analogs. In the LRHS, this difference comes from the influence of the higher-order modes of the resonators (Fig. 3(b)-(e)). In the LRPEC, the differences are larger because not only is there influence from these higher-order modes but there are also 3D effects from the matrix physical realization, which are more significant at higher frequencies (Fig. 2(b)). Zooming into the vicinity of the lower edge of the band gap of the LREPC (Fig. 4(c) – inset), there is not a single sharp drop in transmission but a series of consecutive smaller transmission drops. This is because of the slight differences in resonance frequency among resonators. These details are specific to the realization of LREPCs because of the difference in geometry of the resonators and don't typically arise in Cartesian locally resonant systems.

Even though there are differences between the 1D and 3D models, the main features of the systems are captured. First, the drop in transmission of the LREPC for frequency ranges agrees well with the band gap predicted from Bloch analysis, which is evidence of the effective periodicity. And second, the LRHS shows a resonant peak inside the band gap of the LREPC. This is a result of its lack of effective periodicity. Thus, we consider our physical implementation of the 1D model successful and use this model for experimental validation.

4. Fabrication and material characterization

We fabricate the 3D-LRHS and 3D-LRPEC using voxel-based additive manufacturing for the matrix and the soft rings and machined steel rings for the moment of inertia. We use a Stratasys Object260 Connex3 3D printer and choose VeroWhite for the matrix material and FLX9895 (digital material that combines VeroWhite and TangoBlack) for the soft ring (Fig. 5(a)). We use a "matte" finish on all parts, which covers the part surfaces with support material, minimizing unnecessary curing due to extra UV exposure intended for other parts in the platform. However, such effects may still be present [40]. A groove is printed in the rubber layers and machined in

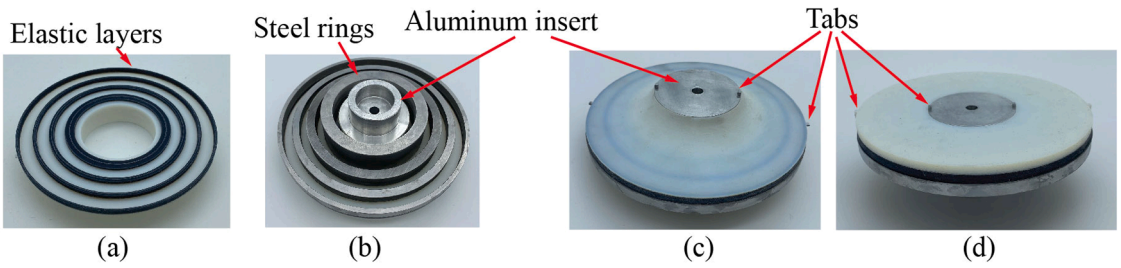

Fig. 5. Sample fabrication. (a) Bottom view of LREPC as printed. (b) Bottom view of LREPC after attaching steel rings and aluminum insert. (c) Top view of LREPC. (d) Top view of LRHS.

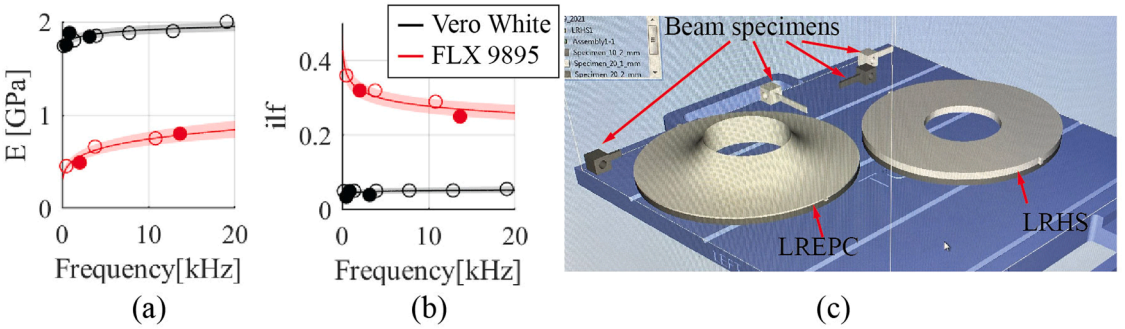

Fig. 6. Characterization of constitutive materials. (a) Young's modulus. (b) Isotropic loss factor. (c) Configuration of the print bed.

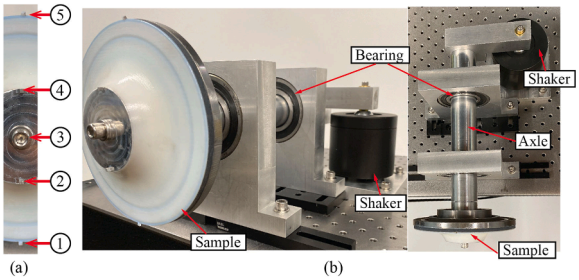

Fig. 7. (a) Points of laser measurement. (b) Experimental setup for measurement of radial torsional wave transmission.

steel to ensure the proper alignment of soft and stiff rings. The steel rings are adhered to the soft ring by using a two-part epoxy (Fig. 5 (b)). An aluminum insert is machined and adhered to the internal radius of the matrix also using a two-part epoxy (Fig. 5(b)). The inset and the matrix have two tabs each (Fig. 5(c-d)), one on each side of their center axis, where measurement points will be located to experimentally obtain transmission (Section 5).

Although the dynamic mechanical analysis of materials like VeroWhite, a few digital materials, and TangoBlack has been reported [41], studies show they can be strongly dependent on UV light exposure times while printing [40] and material expiration date [42]. In fact, reported material properties in the literature are quite variable. For example, reported Young's modulus of VeroWhite can range from 1.2GPa [40] up to 3GPa [43], which even falls outside the 2-3 GPa range reported by Stratasys [44]. Thus, to meaningfully experimentally validate the LREPC and LRHS designs, and to understand the possible effects of viscoelasticity in their response, we characterize the constitutive materials. To do so, we print beam specimens of different lengths in the same print bed as the samples (Fig. 6(c)). We use the Archimedes method to measure density and a modified ASTM E756 [11,35] to characterize the viscoelastic properties of VeroWhite and FLX9895 (Fig. 6(a)-(b)). We use an exponential fit on the data at discrete frequencies to extract the material property dependence on frequency, which are then used as inputs to the 1D model to calculate transmission numerically (Section 5). It is worth noting the material properties of the beam samples are not expected to exactly match those of the LREPC/LRHS, because the beam specimen, LREPC, and LRHS require a different number of printed layers to be built and thus have different times of UV light exposure [40]. However, because of their similar sizes, we expect this difference to be minimal in the LREPC and LRHS. In fact, we show later that with some adjustment to the material properties obtained from the beam specimens, the predicted behavior from the 1D model accurately fits experimental results of both LRHS and LREPC (Fig. 9(b)).

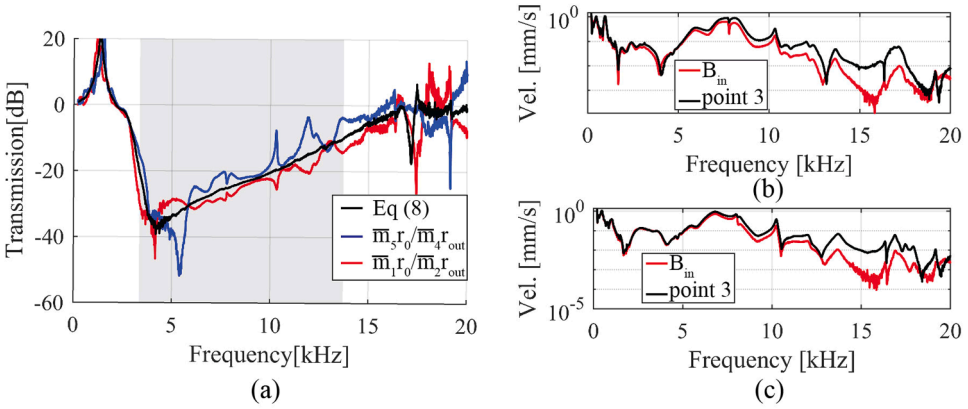

Fig. 8. (a) Transmission of LREPC from the different measured signals. Comparison between measurements of the bending component of velocity on (b) LREPC and (c) LRHS.

5. Experimental validation

5.1. Experimental setup

We introduce here an experimental setup that allows for accurate measurement of transmission of radial torsional waves (Fig. 7). The setup consists of an electrodynamic shaker that imposes torsional waves in a main axle through a connecting arm. The axle sits on a pair of ball bearings to allow it to rotate while reducing bending vibrations. Torsional vibrations travel through the axle and into the sample, which is attached to the shaft through an aluminum insert. A lock-in amplifier generates a sinusoidal input to the shaker. We measure velocity at four measuring points located on tabs on both sides of the sample (Fig. 7(a) - points 1,2,4,5) and one point located in the center of the axle (Fig. 7(a) - point 3) using a single-point laser vibrometer. The lock-in amplifier records the amplitude and phase of the velocity at each measurement point. We sweep through frequencies to obtain the transmission at the different frequencies.

A direct calculation of torsional wave transmission could be done by calculating the ratio of the measured velocities of point 1 to point 2, or of point 5 to point 4 (Fig. 7(a)). However, this measurement of transmission fails to isolate the torsional component of velocity from the bending component of velocity. Although most of the excitation of the shaft (and thus in the sample) is in torsion, there is a bending moment because the applied shaker force is offset from the bearings. The mass of our sample is also localized within a small region at the tip of the axle (Fig. 7(b)), reducing the resonant modes of the axle and promoting bending vibrations. Thus, it is crucial to decouple the torsional and bending components of vibrations to obtain an accurate measurement of torsional transmission, particularly inside a torsional band gap where torsional vibrations at the output can be on the order of the bending vibrations (Section 5.2).

To isolate torsional vibrations, we take measurements on both sides of the main axle (Fig. 7(a)). The signals on points 2 and 4 are used to decouple torsional and bending components of velocity in the inner radius of the sample. Under pure torsion (bending), velocities of point 2 are out-of-phase (in-phase) with respect to velocities of point 4. Thus, if both bending and torsional waves are present, the signal of point 2 is composed of an out-of-phase component (the torsional component) and an in-phase component (the bending component) with respect to point 4. Thus, we can express the measured signals at points 2 and 4 as,

$$\overline{m}_i \sin(\omega t + \phi_i) = A_{in}\sin(\omega t + \psi_{ini}) + B_{in}\sin(\omega t + \psi_{inb}) \tag{6}$$

where $\overline{m}_i$ and ϕ_i are measured amplitude and phase of velocities of point i, respectively, A_{in} and ψ_{ini} are amplitude and phase of the torsional component of tangential velocity at the inner radius, respectively, B_{in} and ψ_{inb} are amplitude and phase of the bending component of tangential velocity at the inner radius, respectively, i takes values of 2 and 4, and $\psi_{in_4} - \psi_{in_2} = \pi$ (because torsional vibrations in point 2 are out-of-phase with respect to torsional vibrations in point 4). All phases are measured with respect to the input signal of the shaker. Similarly, we can take signals of points 1 and 5 and obtain an equivalent equation for bending and torsional components of tangential velocity of the outer radius,

$$\overline{m}_j \sin(\omega t + \phi_i) = A_{out}\sin(\omega t + \psi_{outi}) + B_{out}\sin(\omega t + \psi_{outb}) \tag{7}$$

where j takes values of 1 and 5 and subscript *out* refers to the outer radius. From Eqs. 6 and 7 and with some algebraic manipulation, the pure torsional component of transmission from the measured signals can be calculated as,

$$T = \frac{r_0 A_{out}}{r_{out} A_{in}} = \frac{r_{in}\sqrt{\overline{m}_1^2 + \overline{m}_5^2 - 2\overline{m}_1\overline{m}_5(\sin(\phi_1)\sin(\phi_5) + \cos(\phi_1)\cos(\phi_5))}}{r_{out}\sqrt{\overline{m}_2^2 + \overline{m}_4^2 - 2\overline{m}_2\overline{m}_4(\sin(\phi_2)\sin(\phi_4) + \cos(\phi_2)\cos(\phi_4))}} \tag{8}$$

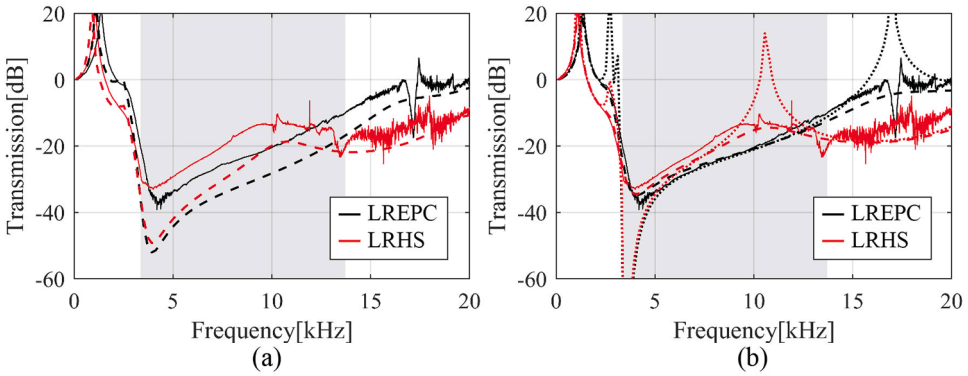

Fig. 9. Measured (solid) and calculated transmission from axisymmetric 1D models (dashed) using properties from material characterization (a) and adjusted properties (b). Dotted curves in (b) show the transmission when the damping of the materials is neglected.

where T is the transmission of radial torsional waves. Note that A_{out} and A_{in} are tangential velocities, thus we must multiply by the ratio of inner to outer radii to obtain transmission in terms of angular velocities as it was defined in Section 1. From Eq. (6) and similar algebraic treatment we can calculate the bending component of velocity at the inner radius,

$$B_{in} = \sqrt{\overline{m}_2^2 + A_{in}^2 - 2\overline{m}_2 A_{in}(\sin(\phi_2)\sin(\psi_{in_2}) + \cos(\phi_2)\cos(\psi_{in_2}))} \tag{9}$$

This bending component can also be measured directly by pointing the laser at the center of the axle (point 3 in Fig. 7(a)). Direct measurements on point 3 and B_{in} should be the same for all frequencies, thus, we compare these signals as validation of the data postprocessing.

5.2. Validation of data postprocessing and effects of bending vibrations

Fig. 8(b-c) compares B_{in} (Eq. 9) with velocities directly measured on point 3. Overall, the two curves agree over a broad frequency range, confirming the signal processing approach accurately decouples the torsional and bending components of the response. The differences at the higher frequencies possibly arise from the low amplitude of excitation that the shaker can exert at these frequencies. This results in a lower signal-to-noise ratio in these frequency ranges, (see Fig. 8(a)) resulting in some difference between the two measured bending amplitudes.

To show the importance of decoupling torsional and bending motion in the measurement of torsional transmission, we compare experimental transmission calculated from Eq. (8) with those calculated from ratios of the raw signal amplitudes (i.e. $\overline{m}_5 r_0 \ / \overline{m}_4 r_{out}$ and $\overline{m}_1 r_0 / \overline{m}_2 r_{out}$) (Fig. 8(a)). Outside the band gap range, transmission from raw signals shows some differences compared to those calculated from Eq. (8). Although these differences look like noise on the transmission curves, they actually come from the measured bending component of vibration at the measurement points. However, since outside the band gap, torsional vibrations in the output radius are large compared to bending vibrations, the differences between transmission curves are not as significant. This is not the case inside the band gap range where the measurements from raw signals show a large deviation from those from Eq. (8). In the band gap region, the torsional vibrations at the output radius are small, and thus the excited bending modes of the LREPC result in bending amplitudes in the order of the torsional vibrations. Comparing the measured transmission from the raw signal on both sides of the specimen (i.e. $\overline{m}_5 r_0 \ / \overline{m}_4 r_{out}$ and $\overline{m}_1 r_0 / \overline{m}_2 r_{out}$) shows peaks from one side of the sample align with dips from the other side. Bending vibrations on one side (points 5 and 4) are in phase with those on the opposite side (points 1 and 2) while the torsional vibrations on one side are out-of-phase with those of the opposite side. Thus, the bending motion interacts constructively with torsion on one side (points 5 and 4) and destructively on the opposite (points 1 and 2). These large differences in measured transmission show that decoupling torsional waves is important to measure the torsional transmission of the radial waves, particularly for accurate measurements inside the band gap range.

5.3. Experimental Results

Fig. 9(a) shows experimentally measured and numerically calculated transmission for both the LREPC and LRHS, as well as the corresponding analytical band gap regions. The numerical transmission is calculated using characterized material properties from Fig. 6. The experimental transmission curves qualitatively agree with those calculated using the 1D finite element model. The differences in transmission likely come from the dependence of material properties on UV exposure previously discussed in Section 4. To show that the differences in response between the LREPC and LRHS do not arise from possible differences in material properties among the two samples, we adjust the material properties of the 1D model. We iterate until 1D transmission curves of both LREPC and LRHS result in a good fit for the same set of material properties. By increasing the stiffness of VeroWhite by 60%, decreasing the stiffness of FLX9895 by 5%, and increasing the isotropic loss factor of FLX9895 by 30%, the experimental transmission of both the LREPC and

LRHS show very good agreement with their respective numerical predictions (Fig. 9(b)). It is expected that the correction factors are different for the two materials because (1) even though FLX9895 has VeroWhite as one of its components, this material is mainly composed of TangoBlack, and (2) the UV light exposure times of FLX9895 and VeroWhite are different because of the differences in geometry of the sections printed with each material. These differences in material properties are consistent with the literature and even after applying the correction factors, the properties fall within reported ranges in the literature [40,43,44]. The results suggest that the materials in the LREPC and LRHS have similar material properties, thus, the difference in behavior is due to the effective periodicity of the LREPC.

The main differences between the responses of the LREPC and LRHS are well captured by the experimental results. There is good agreement between the transmission drop in the LREPC and the band gap regions, which is experimental evidence that the LREPC behaves as an effectively periodic locally resonant system. This is not the case for the LRHS, where there is an increase in transmission inside the band gap region and a shift towards lower frequencies at the lower edge of the band gap. The increase in transmission comes from a resonance of the LRHS inside the band gap region and is actually attenuated due to damping of the constituent materials, but this would be higher in materials with lower damping. This can be more clearly seen if we calculate 1D transmission of the LREPC and LRHS assuming no damping for neither VeroWhite nor FLX9895 materials (Fig. 9(b)-dotted). In the LRHS, the attenuated resonance inside the band gap in the damped system is a sharp peak in the undamped system (see the peak in transmission around 11kHz in Fig. 9 (b)). This shows that there is indeed a resonance frequency of the LRHS inside the predicted band gap range. However, no peaks are found inside the band gap for the undamped LREPC. Essentially, the band gaps of the LREPC predicted from Bloch analysis do not apply to the LRHS.

These experiments provide evidence that LREPCs are needed to obtain behaviors predicted by band structure. To apply concepts of AMs that arise from their band structure to radial waves, effective periodicity of the underlying media must be used. In addition, the LREPC is more efficient at attenuating vibrations inside the band gap range compared to the LRHS, at the same static torsional stiffness. Thus, if there is a particular stiffness requirement for a certain engineering application, the LREPC outperforms the LRHS in terms of vibration attenuation.

6. Conclusion

In this paper, we physically realize the concept of effective periodicity introduced in previous studies [28]. A radial variation in out-of-plane thickness results in the required radial variation of impedance, resulting in effective periodicity. We experimentally demonstrate effective periodicity in an LREPC, which also includes the realization of local torsional resonances; however, a similar approach can be used to realize an EPC. Emulating the realization of local resonances on a Cartesian locally resonant system, we implement the concept of torsional resonances using soft, light rings to connect a series of heavy, stiff rings to the matrix of the LREPC. Different from a Cartesian system, the physical realization of resonators in an LREPC requires different geometries among resonators, i.e. there is an additional effective periodicity that arises from the resonator design. We thoroughly study the response of the thickness varying matrix as well as the geometrically different resonators to explain the slight differences found between the axisymmetric 1D model and the physical model.

We fabricate an LREPC and an LRHS, a system with geometric periodicity but no effective periodicity, using voxel-based additive manufacturing and machined steel rings. We test the fabricated samples with an experimental setup that can excite radial torsional waves and decouple the measured torsional vibrations from bending vibrations through postprocessing multiple measurement locations to obtain an accurate measure of transmission of radial torsional waves. Agreement between experimental transmission of the LREPC and band gap ranges shows evidence that we have physically realized effective periodicity. Furthermore, the experimental results show the LREPC is more efficient than the LRHS at attenuating vibration inside the band gap, and that in the absence of effective periodicity, the response of the LRHS system deviates from the response predicted by the band structure.

Our results provide experimental evidence that effective periodicity is required to obtain canonical properties of AMs for radially propagating waves. Although here we focus on torsional waves, our studies motivate realizing effective periodicity in other polarization directions or even other ways of realization. Given their possible application in rotating equipment such as turbines, compressors, gears, or engines, future work may include the effects of rotation on LREPCs and EPCs. Our experimental results show that these systems can be used to provide new ways to reduce noise and damage in components that suffer from torsional vibrations.

CRediT authorship contribution statement

Ignacio Arretche: Conceptualization, Data curation, Formal analysis, Investigation, Methodology, Software, Validation, Visualization, Writing – original draft, Writing – review & editing. **Kathryn H. Matlack:** Conceptualization, Funding acquisition, Investigation, Project administration, Supervision, Writing – review & editing.

Declaration of Competing Interest

The authors declare that they have no known competing financial interests or personal relationships that could have appeared to influence the work reported in this paper.

Data availability

Data will be made available on request.

Acknowledgment

This material is based upon work supported by the National Science Foundation under Grant No. CMMI-2031110. The authors would also like to acknowledge Prof. Kai James and his students, Lee Alcoque and Anurag Bhattacharyya, for their assistance in the fabrication of the samples.

Appendix A

Table A1 shows the summary of all the cases studied in the paper.

Table A1
Summary of cases studied.

Case	Schematic	Matrix properties	Resonators	Equations
Matrix1D		$\mu(r) = \mu_0/r^3$ $\rho(r) = \rho_0/r^3$ $h(r) = h_0$	No resonators	1D (Eq. (1))
MatrixThickness		$\mu(r) = \mu_0$ $\rho(r) = \rho_0$ $h(r) = h_0/r^3$	No resonators	3D $(\sigma_{ij,j} = \rho a_i)$
MatrixMatProp		$\mu(r) = \mu_0/r^3$ $\rho(r) = \rho_0/r^3$ $h(r) = h_0$	No resonators	3D $(\sigma_{ij,j} = \rho a_i)$
MatrixHomog		$\mu(r) = \mu_0$ $\rho(r) = \rho_0$ $h(r) = h_0$	No resonators	3D $(\sigma_{ij,j} = \rho a_i)$
1D LREPC		$\mu(r) = \mu_0/r^3$ $\rho(r) = \rho_0/r^3$ $h(r) = h_0$	Lumped spring-mass	1D (Eq. (1))
1D LRHS		$\mu(r) = \mu_0$ $\rho(r) = \rho_0$ $h(r) = h_0$	Lumped spring -mass	1D (Eq. (1))
3D LREPC		$(r) = \mu_0$ $\rho(r) = \rho_0$ $h(r) = h_0/r^3$	3D physical (Fig. 3)	3D $(\sigma_{ij,j} = \rho a_i)$
3D LRHS	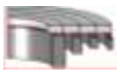	$(r) = \mu_0$ $\rho(r) = \rho_0$ $h(r) = h_0$	3D physical (Fig. 3)	3D $(\sigma_{ij,j} = \rho a_i)$

References

[1] M.I. Hussein, M.J. Leamy, M. Ruzzene, Dynamics of phononic materials and structures: historical origins, recent progress, and future outlook, Appl. Mech. Rev. 66 (4) (2014), 040802, https://doi.org/10.1115/1.4026911.
[2] M. Sigalas, E.N. Economou, Band structure of elastic waves in two dimensional systems, Solid State Commun. 86 (3) (1993) 141–143, https://doi.org/10.1016/0038-1098(93)90888-T.

[3] M.S. Kushwaha, P. Halevi, L. Dobrzynski, B. Djafari-Rouhani, Acoustic band structure of periodic elastic composites, Phys. Rev. Lett. 71 (13) (1993) 2022–2025, https://doi.org/10.1103/PhysRevLett.71.2022.
[4] R. Zhu, X.N. Liu, G.K. Hu, C.T. Sun, G.L. Huang, Negative refraction of elastic waves at the deep-subwavelength scale in a single-phase metamaterial, Nat. Commun. 5 (1) (2014) 5510, https://doi.org/10.1038/ncomms6510.
[5] Z. Liu, X. Zhang, Y. Mao, Y.Y. Zhu, Z. Yang, C.T. Chan, P. Sheng, Locally resonant sonic materials, Science 289 (5485) (2000) 1734–1736, https://doi.org/10.1126/science.289.5485.1734, 80-.
[6] M. Xiao, G. Ma, Z. Yang, P. Sheng, Z.Q. Zhang, C.T. Chan, Geometric phase and band inversion in periodic acoustic systems, Nat. Phys. 11 (3) (2015) 240–244, https://doi.org/10.1038/NPHYS3228.
[7] J. Yin, M. Ruzzene, J. Wen, D. Yu, L. Cai, L. Yue, Band transition and topological interface modes in 1D elastic phononic crystals, Sci. Rep. 8 (2018) 6806, https://doi.org/10.1038/s41598-018-24952-5.
[8] A.S. Phani, J. Woodhouse, N.A. Fleck, Wave propagation in two-dimensional periodic lattices, J. Acoust. Soc. Am. 119 (4) (2006) 1995–2005, https://doi.org/10.1121/1.2179748.
[9] C.D. Pierce, C.L. Willey, V.W. Chen, J.O. Hardin, J.D. Berrigan, A.T. Juhl, K.H. Matlack, Adaptive elastic metastructures from magneto-active elastomers, Smart Mater. Struct. 29 (6) (2020), 065004, https://doi.org/10.1088/1361-665X/ab80e4.
[10] K.H. Matlack, A. Bauhofer, S. Krödel, A. Palermo, C. Daraio, Composite 3D-printed metastructures for low-frequency and broadband vibration absorption, in: 113, 2016, pp. 8386–8390, https://doi.org/10.1073/pnas.1600171113.
[11] I. Arretche, K.H. Matlack, Experimental testing of vibration mitigation in 3D-printed architected metastructures, J. Appl. Mech. 86 (11) (2019), https://doi.org/10.1115/1.4044135.
[12] B. Liang, X.S. Guo, J. Tu, D. Zhang, J.C. Cheng, An acoustic rectifier, Nat. Mater. 9 (12) (2010) 989–992, https://doi.org/10.1038/nmat2881.
[13] G. Ma, C. Fu, G. Wang, P. Del Hougne, J. Christensen, Y. Lai, P. Sheng, Polarization bandgaps and fluid-like elasticity in fully solid elastic metamaterials, Nat. Commun. 7 (1) (2016) 1–8, https://doi.org/10.1038/ncomms13536.
[14] V. Zega, P.B. Silva, M.G.D. Geers, V.G. Kouznetsova, Experimental proof of emergent subharmonic attenuation zones in a nonlinear locally resonant metamaterial, Sci. Rep. 10 (1) (2020) 1–11, https://doi.org/10.1038/s41598-020-68894-3, 2020 101.
[15] J.D. Hobeck, D.J. Inman, 3D printing of metastructures for passive broadband vibration suppression, in: Proceedings of the 20th International Conference on Composite Materials, Copenhagen, Denmark, 2015, https://doi.org/10.13140/RG.2.1.5003.8489.
[16] K.K. Reichl, D.J. Inman, Lumped mass model of a 1D metastructure for vibration suppression with no additional mass, J. Sound Vib. 403 (2017) 75–89, https://doi.org/10.1016/j.jsv.2017.05.026.
[17] L. D'Alessandro, E. Belloni, R. Ardito, A. Corigliano, F. Braghin, Modeling and experimental verification of an ultra-wide bandgap in 3D phononic crystal, Appl. Phys. Lett. 109 (22) (2016), 221907, https://doi.org/10.1063/1.4971290.
[18] F.R. Montero De Espinosa, E. Jiménez, M. Torres, Ultrasonic band gap in a periodic two-dimensional composite, Phys. Rev. Lett. 80 (6) (1998) 1208–1211, https://doi.org/10.1103/PhysRevLett.80.1208.
[19] H.J. Lee, J.R. Lee, S.H. Moon, T.J. Je, E.C. Jeon, K. Kim, Y.Y. Kim, Off-centered double-slit metamaterial for elastic wave polarization anomaly, Sci. Rep. 7 (1) (2017) 1–13, https://doi.org/10.1038/s41598-017-15746-2, 2017 71.
[20] S. Haisheng, D. Liqiang, L. Shidan, L. Wei, L. Shaogang, W. Weiyuan, S. Dongyan, Z. Dan, Propagation of torsional waves in a thin circular plate of generalized phononic crystals, J. Phys. D. Appl. Phys. 47 (29) (2014), 295501, https://doi.org/10.1088/0022-3727/47/29/295501.
[21] P. Yeh, A. Yariv, E. Maron, Theory of bragg fiber, J. Opt. Soc. Am. 68 (9) (1978) 1196–1201, https://doi.org/10.1364/JOSA.68.001196.
[22] H. Shu, L. Zhao, X. Shi, W. Liu, D. Shi, F. Kong, Torsional wave propagation in a circular plate of piezoelectric radial phononic crystals, J. Appl. Phys. 118 (2015), 184904, https://doi.org/10.1063/1.4935451.
[23] E. Manconi, S.V. Sorokin, R. Garziera, M.M. Quartaroli, Free and forced wave motion in a two-dimensional plate with radial periodicity, Appl. Sci. 11 (22) (2021) 10948, https://doi.org/10.3390/APP112210948, 2021, Vol. 11, Page 10948.
[24] Z. Xu, F. Wu, Z. Guo, Low frequency phononic band structures in two-dimensional arc-shaped phononic crystals, Phys. Lett. A 376 (33) (2012) 2256–2263, https://doi.org/10.1016/j.physleta.2012.05.037.
[25] T. Ma, T. Chen, X. Wang, Y. Li, P. Wang, Band structures of bilayer radial phononic crystal plate with crystal gliding, J. Appl. Phys. 116 (2014), 104505, https://doi.org/10.1063/1.4895138.
[26] D. Torrent, J. Sánchez-Dehesa, Radial wave crystals: radially periodic structures from anisotropic metamaterials for engineering acoustic or electromagnetic waves, Phys. Rev. Lett. 103 (6) (2009), 064301, https://doi.org/10.1103/PhysRevLett.103.064301.
[27] I. Arretche, K.H. Matlack, Effective phononic crystals for non-cartesian elastic wave propagation, Phys. Rev. B 102 (13) (2020), 134308, https://doi.org/10.1103/PhysRevB.102.134308.
[28] I. Arretche, K.H. Matlack, Locally resonant effective phononic crystals for subwavelength vibration control of torsional cylindrical waves, J. Vib. Acoust. 144 (3) (2022), 031007, https://doi.org/10.1115/1.4052748.
[29] J. Carbonell, A. Díaz-Rubio, D. Torrent, F. Cervera, M.A. Kirleis, A. Piqué, J. Sánchez-Dehesa, Radial photonic crystal for detection of frequency and position of radiation sources, Sci. Rep. 2 (2012) 558, https://doi.org/10.1038/srep00558.
[30] Torrent, D., and Sánchez-Dehesa, J., 2022, "Anisotropic mass density by radially periodic fluid structures" DOI: 10.1103/PhysRevLett.105.174301.
[31] J.C. Wachel, F.R. Szenasi, Analysis of torsional vibrations in rotating machinery, in: Proceedings of the Twenty-Second Turbomachinery Symposium, 1993, pp. 127–151.
[32] L. Li, A. Cai, Low-frequency band gap mechanism of torsional vibration of lightweight elastic metamaterial shafts, Eur. Phys. J. Appl. Phys. 75 (2016) 10501, https://doi.org/10.1051/epjap/2016160169.
[33] Y. Xiao, J. Wen, X. Wen, Analysis and enhancement of torsional vibration stopbands in a periodic shaft system, J. Phys. D Appl. Phys. 46 (2013), 145306, https://doi.org/10.1088/0022-3727/46/14/145306.
[34] J. Cabaret, P. Béquin, G. Theocharis, V. Andreev, V.E. Gusev, V. Tournat, Nonlinear hysteretic torsional waves, Phys. Rev. Lett. 115 (2015), 054301, https://doi.org/10.1103/PhysRevLett.115.054301.
[35] ASTM International, Standard Test Method for Measuring Vibration- Damping Properties of Materials, ASTM International, West Conshohocken, PA, 2017, https://doi.org/10.1520/E0756-05R17. ASTM Standard E756.
[36] T. Miles, M. Lucas, N. Halliwell, S. Rotherber, Torsional and bending vibration measurement on rotors using laser technology, J. Sound Vib. 226 (3) (1999) 441–467, https://doi.org/10.1006/jsvi.1999.2253.
[37] T.A. Schaedler, W.B. Carter, Architected cellular materials, Annu. Rev. Mater. Res. 46 (1) (2016) 187–210, https://doi.org/10.1146/annurev-matsci-070115-031624.
[38] X. Zheng, H. Lee, T.H. Weisgraber, M. Shusteff, J. DeOtte, E.B. Duoss, J.D. Kuntz, M.M. Biener, Q. Ge, J.A. Jackson, S.O. Kucheyev, N.X. Fang, C.M. Spadaccini, Ultralight, ultrastiff mechanical metamaterials, Science 344 (6190) (2014) 1373–1377, https://doi.org/10.1126/science.1252291.
[39] W. Zunker, S. Gonella, Soft topological lattice wheels, Extrem. Mech. Lett. 46 (2021), 101344, https://doi.org/10.1016/J.EML.2021.101344.
[40] M.W. Barclift, C.B. Williams, Examining variability in the mechanical properties of parts manufactured via polyjet direct 3D printing, in: Proceedings of the International Solid Freeform Fabrication Symposium, 2012, pp. 6–8.
[41] K.K. Reichl, &D.J. Inman, Dynamic mechanical and thermal analyses of objet connex 3D printed materials, Exp. Tech. 42 (2018) 19–25, https://doi.org/10.1007/s40799-017-0223-0.

[42] J. Mueller, K. Shea, C. Daraio, Mechanical properties of parts fabricated with inkjet 3D printing through efficient experimental design, Mater. Des. 86 (2015) 902–912, https://doi.org/10.1016/j.matdes.2015.07.129.
[43] T. Stankovic, J. Mueller, P. Egan, K. Shea, A generalized optimality criteria method for optimization of additively manufactured multimaterial lattice structures, J. Mech. Des. Trans. ASME 137 (11) (2015), https://doi.org/10.1115/1.4030995/474762.
[44] 2022, "Vero material data sheet" [Online]. Available: https://www.stratasys.com/-/media/files/material-spec-sheets/mds_pj_vero_for_j55_0320a.pdf. [Accessed: 04-Aug-2022].